European Journal of Mechanics / B Fluids 67 (2018) 1–14

Contents lists available at ScienceDirect

European Journal of Mechanics / B Fluids

journal homepage: www.elsevier.com/locate/ejmflu

Nonlinear corrections of linear potential-flow theory of ship waves

Chao Ma [a,b], Yi Zhu [a,b], Jiayi He [c], Chenliang Zhang [c], Decheng Wan [a,b], Chi Yang [d], Francis Noblesse [a,b,*]

[a] State Key Laboratory of Ocean Engineering, School of Naval Architecture, Ocean & Civil Engineering, Shanghai Jiao Tong University, Shanghai, China
[b] Collaborative Innovation Center for Advanced Ship and Deep-Sea Exploration, Shanghai Jiao Tong University, Shanghai, China
[c] Marine Design and Research Institute of China, Shanghai, China
[d] Department of Physics and Astronomy, George Mason University, Fairfax, Virginia, USA

HIGHLIGHTS

- Nonlinear effects on sinkage, trim, wave drag and wave profiles are relatively small.
- An important exception is the wave drag of ships with bulbous bows.
- Predictions of NM theory with nonlinear corrections agree well with experiments.

ARTICLE INFO

Article history:
Received 1 June 2017
Received in revised form 11 July 2017
Accepted 12 July 2017
Available online 31 July 2017

Keywords:
Ship waves
Linear potential flow
Nonlinearities
Sinkage, trim, drag
Wave profiles

ABSTRACT

The Neumann–Michell (NM) theory – a practical linear potential flow theory – is applied to four freely-floating ship models (Wigley, S60, DTMB5415, KCS), assumed to advance at a constant speed in calm water of large depth, to investigate nonlinear effects on the wave drag, the sinkage, the trim, and the wave profile along the hull, and to approximately account for these effects via simple corrections of the linear theory. Nonlinear effects are found to be relatively small. However, an important exception to this general finding is that the wave drag of a bulbous ship (DTMB5415, KCS) is greatly reduced due to the nonlinear component of the pressure in the Bernoulli relation. This important nonlinear effect is readily included in the NM theory. The nonlinear component of the pressure in the Bernoulli relation also yields a small increase of the sinkage, likewise readily included in the NM theory. Moreover, free-surface nonlinearities can have appreciable, although not large, effects on the wave profile. These nonlinear effects can also be approximately taken into account via a simple transformation of the linear wave profile. Indeed, the flow computations for the four ship models considered here suggest that simple (post-processing) nonlinear corrections (that require no additional flow computations) of the NM theory yield numerical predictions of the wave drag, the sinkage, the trim and the wave profile that agree well with experimental measurements, and compare favorably with predictions given by more complex computational methods.

1. Introduction

Nonlinear effects on the flow around a ship that advances at a constant speed in calm water of large depth and lateral extent are considered. The influence of nonlinearities is readily apparent from a ship bow wave, where wavebreaking or overturning thin sheets of water are commonly observed [1,2]. Such nonlinear effects cannot be directly modeled within the framework of linear potential flow theory. In particular, linear potential flow theory cannot predict the occurrence of wavebreaking, although it arguably may be less ill suited than nonlinear potential flow theory to represent highly nonlinear effects associated with wavebreaking or overturning waves at a ship bow. Wavebreaking can in principle be modeled within the framework of CFD methods that solve the unsteady Reynolds-averaged Navier–Stokes equations (URANS), although the difficulties are considerable. Moreover, CFD methods based on the URANS are ill suited and unnecessary for routine practical applications to ship design and hull-form optimization, for which linear potential flow theory is adequate and most useful. Indeed, linear potential flow theory – specifically the Neumann–Michell (NM) theory considered here – is practical and yields predictions of the sinkage, the trim, the drag and wave profiles that are in satisfactory agreement with experimental measurements as well as numerical predictions obtained via alternative, considerably more complex, computational methods, as is shown in several studies listed below.

* Corresponding author.
E-mail address: noblfranc@gmail.com (F. Noblesse).

http://dx.doi.org/10.1016/j.euromechflu.2017.07.006
0997-7546/

The NM theory is based on the usual Kelvin–Michell linearized free-surface boundary condition. Main features of that theory, expounded in [3,4], are summarized in [5] and are only briefly noted here. The NM theory is a modification of the well-known Neumann–Kelvin (NK) theory. In particular, the NM theory does not involve a line integral around the ship waterline, unlike the NK theory, and is based on a consistent linear flow model, whereas [3] argues that the NK theory does not correspond to a consistent linear flow model. Main features of the NM theory are considered in [6–9], and validation studies and applications are reported in [4,5,10–14]. In particular, [14] shows that the influence of sinkage and trim on the drag of a common monohull ship at Froude numbers $F \leq 0.45$ can easily and realistically be evaluated via the NM theory. A notable useful feature of this theory is that it is well suited for routine practical applications to ship design and hull-form optimization, as is amply demonstrated in [15–23]. Indeed, the NM theory yields realistic flow predictions, sufficiently accurate for hydrodynamic optimization, in a very practical way. In particular, the NM theory makes it possible to evaluate the pressure distribution at a ship hull surface in about 1s using a common PC.

This practical linear potential flow theory is used here to analyze the influence of nonlinear effects on the sinkage, the trim, the wave drag and the wave profile along the ship hull, and to approximately account for these nonlinear effects via simple corrections of the linear theoretical predictions (without additional flow computations). Nonlinear effects on the wave drag, the trim, the sinkage and the wave profile are found to be relatively small. An exception to this general finding is that the wave drag of a ship with a large bulb is greatly reduced due to the nonlinear component of the pressure in the Bernoulli relation. This important nonlinear effect on the wave drag is readily taken into account within the NM theory. In addition, the nonlinear component of the pressure in the Bernoulli relation yields an increase of the sinkage. This relatively small but appreciable nonlinear effect is also readily included within the NM theory. Moreover, free-surface nonlinearities can have appreciable, although not large, effects on the wave profile. These nonlinear effects on the wave profile can also be approximately taken into account via a simple correction of the linear wave profile.

Four freely-floating ship models (Wigley, S60, DTMB5415, KCS) are considered here for purposes of illustration and validation. Side views and bottom views of these four well-known models are depicted in Fig. 1. Numerical predictions of the sinkage, the trim, the wave drag and wave profiles are compared with experimental measurements reported in the literature.

Specifically, for the Wigley hull, the six sets of experimental measurements of sinkage, trim and residuary drag performed at IHHI (Ishikawajima-Harima Heavy Industries), SRI (Ship Research Institute), UT (University of Tokyo) and YNU (Yokohama National University), and the two sets of experimental measurements of wave profiles at six Froude numbers within the range $0.25 \leq F \leq 0.408$ performed at UT and SRI, are used here. These experimental measurements are reported in [24–26].

For the S60 ship model, the seven sets of measurements of sinkage, trim and residuary drag performed at IHHI, UT, SRS (Ship Research Station), UH (University of Hiroshima) and SSSRI (Shanghai Ship & Shipping Research Institute), and the three sets of measurements of wave profiles at eleven Froude numbers within the range $0.18 \leq F \leq 0.35$ performed at UT, SRS and SNU (Seoul National University), are used. These experimental data are reported in [26–28].

For the DTMB5415 model, the three sets of measurements of sinkage, trim, residuary drag and wave profiles (for $F = 0.28$ and $F = 0.41$) performed at DTMB (David Taylor Model Basin), INSEAN (Instituto Nazionale Per Studi Ed Esperienze Di Architettura Navale) and IIHR (Iowa Institute of Hydraulic Research) and reported in [29–31] are used.

Finally, for the KCS ship model, the two sets of measurements of sinkage, trim and residuary drag performed at MOERI (Maritime Ocean Engineering Research Institute) and NMRI (National Maritime Research Institute) and reported in [29–31], and the experimental wave profiles (for $F = 0.26$) measured at MOERI and reported in [32,33], are used.

The flow computations for the four ship models considered here suggest that simple (post-processing) nonlinear corrections (that require no additional flow computations) of the NM linear theory yield numerical predictions of the wave drag, the sinkage, the trim and the wave profile that agree well with experimental measurements, and compare favorably with predictions given by more complex computational methods.

2. Pressure

Potential flow around the mean wetted hull surface Σ^H of a ship, of length L, that advances at a constant speed V in calm water of effectively infinite depth and lateral extent is considered. Coordinates and flow variables are made nondimensional with respect to the gravitational acceleration g, the water density ρ, and the length L and the speed V of the ship. The Froude number is defined as $F \equiv V/\sqrt{gL}$. The flow is observed from a Cartesian system of nondimensional coordinates $\mathbf{x} \equiv (x, y, z) \equiv \mathbf{X}/L$ attached to the moving ship, and is then steady (independent of time). The x axis is chosen along the path of the ship and points toward the ship bow. The undisturbed free surface is taken as the plane $z = 0$ and the z axis points upward. The ship bow and stern are located at $(0.5, 0, 0)$ and $(-0.5, 0, 0)$. The flow velocity is given by $(\phi_x - 1, \phi_y, \phi_z)$ where $(\phi_x, \phi_y, \phi_z) \equiv (\Phi_X, \Phi_Y, \Phi_Z)/V$ denotes the velocity of the flow created by the ship and $\phi \equiv \Phi/(VL)$ is the flow potential. The unit vector $\mathbf{n} \equiv (n^x, n^y, n^z)$ is normal to the ship hull surface Σ^H and points outside the ship (into the water).

The nondimensional flow pressure p at the ship hull surface Σ^H is determined from the Bernoulli relation

$$p \equiv (P - P_a)/(\rho V^2) = p^* - z/F^2 \tag{1a}$$

where P_a denotes the atmospheric pressure, and p^* is the hydrodynamic pressure

$$p^* = \phi_x - (\phi_x^2 + \phi_y^2 + \phi_z^2)/2. \tag{1b}$$

The linear approximation ϕ_x to the pressure p^* is denoted as $\widetilde{p^*} \equiv \phi_x$ hereafter.

The velocity components (ϕ_x, ϕ_y, ϕ_z) at a ship hull surface Σ^H can be expressed in terms of the velocity component ϕ_n along the unit vector $\mathbf{n}$ normal to Σ^H and the velocity components ϕ_d and ϕ_t along two unit vectors $\mathbf{d}$ and $\mathbf{t}$ tangent to Σ^H. The unit vectors $\mathbf{d}$ and $\mathbf{t}$ are chosen as

$$\mathbf{d} \equiv \frac{[\,0, -n^z, -n^y\,]}{\sqrt{(n^y)^2 + (n^z)^2}} \quad \text{and} \quad \mathbf{t} \equiv \frac{[(n^y)^2 + (n^z)^2, -n^x n^y, -n^x n^z\,]}{\sqrt{(n^y)^2 + (n^z)^2}}$$

here, as in [3]. The three unit vectors $\mathbf{n}$, $\mathbf{d}$ and $\mathbf{t}$ are orthogonal. One then has

$$\phi_x^2 + \phi_y^2 + \phi_z^2 = \phi_n^2 + \phi_t^2 + \phi_d^2 = (n^x)^2 + \phi_t^2 + \phi_d^2$$

where the boundary condition $\phi_n = n^x$ at Σ^H was used, and

$$p^* = \sqrt{(n^y)^2 + (n^z)^2}\,\phi_t + (n^x)^2/2 - (\phi_t^2 + \phi_d^2)/2 \tag{2a}$$

$$\widetilde{p^*} = \phi_x = \sqrt{(n^y)^2 + (n^z)^2}\,\phi_t + (n^x)^2. \tag{2b}$$

The tangential velocity components ϕ_t and ϕ_d are determined hereafter via the Neumann-Michell (NM) theory, as was already

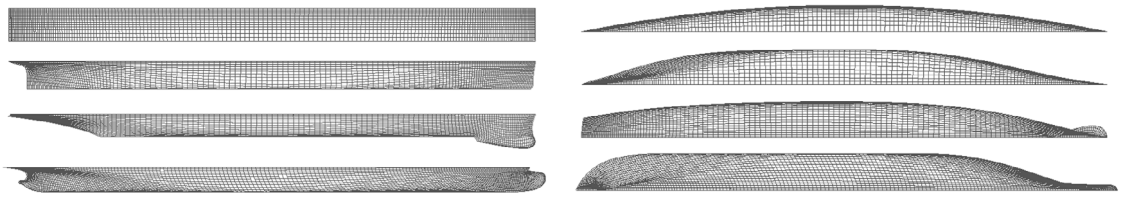

Fig. 1. Side views (left) and bottom views (right) of the mean wetted hull surfaces Σ_0^H of the Wigley (top row), S60 (second row), DTMB5415 (third row) and KCS (bottom row) hulls approximated via 2880 (Wigley), 2880 (S60), 3000 (DTMB5415) or 4776 (KCS) bilinear panels.

noted. Useful insight into the importance of nonlinearities can readily be gained via a comparison of the sinkage, the trim and the drag associated with the hydrodynamic pressure p^* or the related linear approximation $\widetilde{p}^* = \phi_x$. This comparison is now considered.

3. Sinkage, trim and drag

The position of the mean wetted hull surface Σ^H of a ship that advances in calm water at a constant speed V is defined by the midship sinkage H^m and the trim angle τ, which correspond to the vertical displacement at midship $x = 0$ and the rotation angle, measured hereafter in degrees, between the wetted hull surface Σ_0^H of the ship at rest, i.e. for $V = 0$, and the mean wetted hull surface Σ^H of the moving ship. Positive values of H^m or τ correspond to a downward vertical displacement at midship or a bow-up rotation, respectively.

[5] shows that, for a broad range of common monohull ships at Froude numbers $F \leq 0.45$, the midship sinkage H^m and the trim angle τ can be realistically estimated – without flow computations – in terms of F and the beam B, the draft D, the length L and the block coefficient C_b of the ship by means of explicit analytical relations, obtained from an analysis of experimental measurements for 22 models of monohull ships. Specifically, H^m and τ can be estimated via the relations

$$H^m \approx 0.9\sqrt{BD}\,(C_b - 0.13)F^2 \tag{3a}$$

$$\tau \approx \frac{9}{\pi}\frac{\sqrt{BD}}{L}[F_*^2\sqrt{1+F_*^8} - 36\,(C_b - 0.13)F^2] \tag{3b}$$

where $F_* \equiv F/0.33$, and τ is expressed in degrees as was already noted. Alternatively, the midship sinkage H^m and the trim angle τ can be determined numerically via the NM theory applied to the hull surface Σ_0^H of the ship at rest – i.e. without iterative flow computations for a series of hull positions – as is also shown in [5].

Specifically, the midship sinkage H^m and the trim angle τ are determined in [5] and here from the nondimensional hydrodynamic lift $C^z \equiv F^z/(\rho L^2 V^2)$ and pitch moment $C^{zx} \equiv M^{zx}/(\rho L^3 V^2)$, evaluated by means of the NM theory applied to the hull surface Σ_0^H of the ship at rest, via the classical relations

$$\frac{H^m}{L} \approx F^2\,\frac{C^z + \varepsilon_2\,C^{zx}}{a_0(1-\varepsilon_0\,\varepsilon_2)} \quad \text{and} \quad \frac{\pi\,\tau}{180} \approx F^2\,\frac{C^{zx} + \varepsilon_0\,C^z}{a_2(1-\varepsilon_0\,\varepsilon_2)} \tag{4a}$$

where $\varepsilon_0 \equiv a_1/a_0$ and $\varepsilon_2 \equiv a_1/a_2$. Moreover, a_0, a_1 and a_2 denote the nondimensional area of the waterplane W_0^H of the wetted hull surface Σ_0^H and the related moments defined as

$$(a_0, a_1, a_2) \equiv \left(\frac{A_0}{L^2}, \frac{A_1}{L^3}, \frac{A_2}{L^4}\right) \equiv \int_{W_0^H} (1, x, x^2)\,dx\,dy. \tag{4b}$$

The hydrodynamic lift C^z and pitch moment C^{zx} in (4a) are determined via integration of the hydrodynamic pressure p^* over the wetted ship hull surface Σ_0^H of the ship at rest, i.e.

$$(C^z, C^{zx}) = \int_{\Sigma_0^H} (n^z, n^x z - n^z x)\,p^*\,da. \tag{4c}$$

These relations show that the lift C^z and the pitch moment C^{zx} are mostly determined by the pressure distribution p^* over the hull bottom, and consequently are relatively insensitive to the precise position of the ship and the details of the hull geometry. As is noted in [5], this basic property explains why – for a broad range of common monohull ships at moderate Froude numbers – the pressure p^* can be integrated over Σ_0^H instead of Σ^H in (4c), and also explains why the sinkage and the trim can be predicted in terms of the dominant hull-shape parameters B, D, L and C_b related to the overall hull geometry as in the analytical relations (3).

Expressions (4c) for the hydrodynamic lift C^z and the pitch moment C^{zx} also show that integration of the negative pressure component $-|\nabla\phi|^2/2$ over the ship hull bottom, where $n^z \approx -1$ and $n^x \approx 0$, can be expected to result in an appreciable increase in C^z, but only a minor change in C^{zx} because the contributions of the fore (where $0 < x$ and $0 < n^x$) and aft (where $x < 0$ and $n^x < 0$) parts of the hull bottom largely cancel out, as is confirmed by the numerical results considered further on.

The nondimensional wave drag $C^w \equiv D^w/(\rho L^2 V^2)$ is similarly determined via integration of the hydrodynamic pressure p^* over the mean wetted hull surface Σ^H, i.e.

$$C^w = \int_{\Sigma^H} n^x p^*\,da. \tag{5}$$

This expression shows that the wave drag is mostly determined by the pressure distribution over the fore and aft of the ship hull. This well-known basic property explains why (unlike the sinkage and the trim) the wave drag is sensitive to the position of the ship and the details of the hull geometry.

Indeed, [14] shows that the wave drag predicted by the relation (5) where the mean wetted hull surface Σ^H is taken as the wetted hull Σ_0^H of the ship at rest is significantly smaller than the wave drag given by (5) with Σ^H taken as the wetted hulls Σ_1^H or Σ_a^H that correspond to the midship sinkage H^m and the trim angle τ predicted by the relations (4) or (3) associated with numerical computations or experimental measurements. Thus, sinkage and trim have a significant influence on the wave drag, and indeed on the viscous drag as well as is shown in [14]. The analysis of sinkage and trim effects on the drag given in [14] also shows that the wave drags predicted by (5) where Σ^H is taken as the wetted hulls Σ_1^H or Σ_a^H do not differ appreciably. Hereafter, the mean wetted hull surface Σ^H in expression (5) for the wave drag is taken as the hull surface Σ_a^H that corresponds to the sinkage H^m and the trim angle τ predicted by the explicit analytical relations (3).

Expression (5) for the wave drag C^w shows that integration of the negative pressure component $-|\nabla\phi|^2/2$ over the fore and aft of the ship hull surface can be expected to only result in a minor change in C^w because the contributions of the fore (where $0 < n^x$) and aft (where $n^x < 0$) of the hull surface largely cancel out, as is confirmed by the numerical results for the Wigley and S60 ship models considered further on. However, for a ship that has a large bulb, integration of the negative pressure component $-|\nabla\phi|^2/2$ over the front of the bulb (where $n^x \approx 1$) can be expected to result in a significant reduction of the drag, as is illustrated further on for the DTMB5415 and KCS models.

The midship sinkage H^m/L, the trim angle τ and the wave drag C^w are compared to the corresponding linear approximations $\widetilde{H}^m/L, \widetilde{\tau}, \widetilde{C}^w$ in Fig. 2 for the freely-floating Wigley, S60, DTMB5415

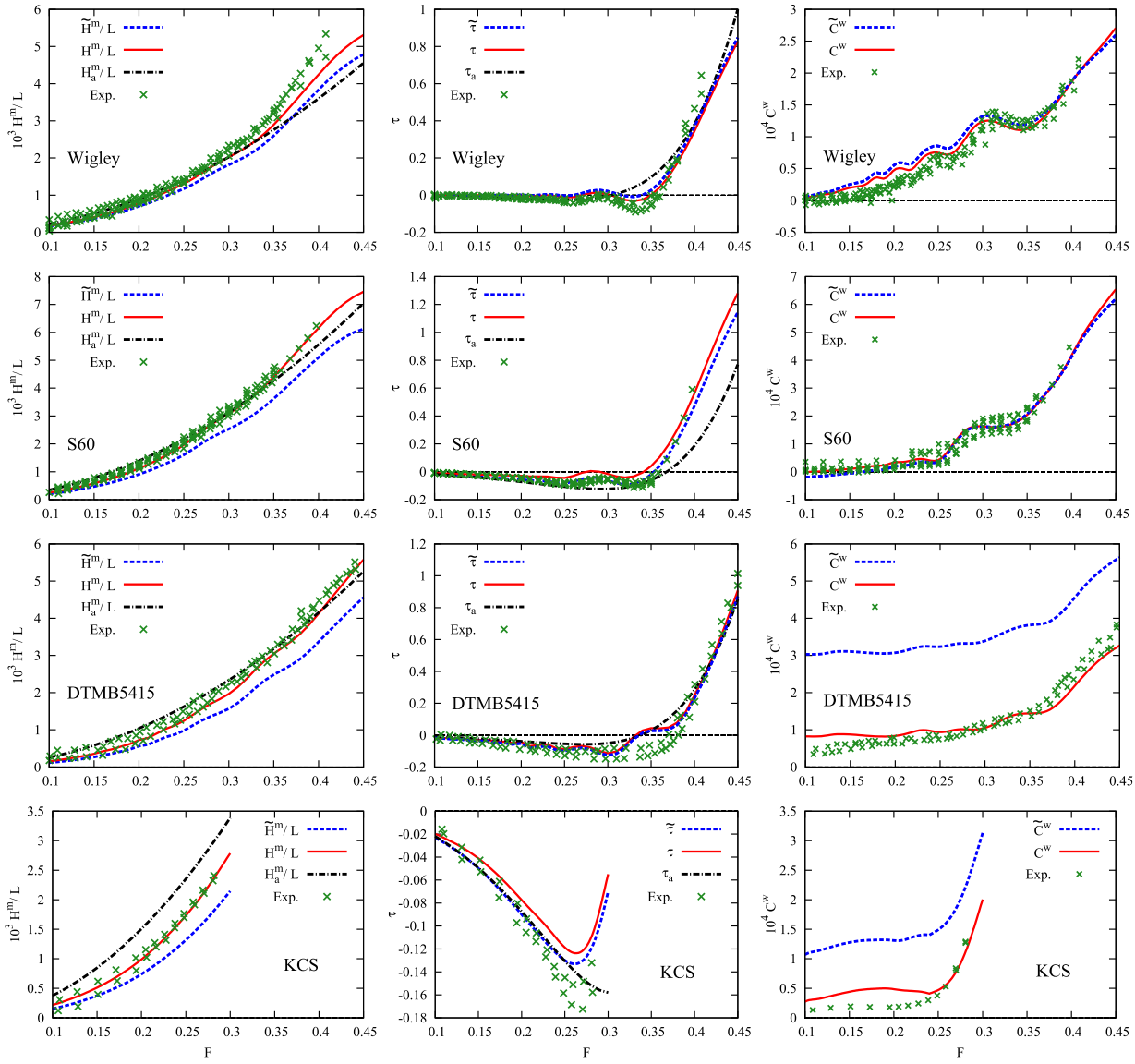

Fig. 2. Midship sinkage H^m/L (left column), trim angle τ (center column) and wave drag C^w (right column) for the freely-floating Wigley (top row), S60 (second row), DTMB5415 (third row) and KCS (bottom row) ship models. $\widetilde{H}^m/L, \widetilde{\tau}, \widetilde{C}^w$ and $H^m/L, \tau, C^w$ correspond to the linear pressure $\widetilde{p}^* = \phi_x$ or the nonlinear pressure $p^* = \phi_x - |\nabla\phi|^2/2$. H_a^m/L and τ_a correspond to the analytical relations (3). Experimental measurements of the residuary drag C^r are depicted as green crosses. (For interpretation of the references to color in this figure legend, the reader is referred to the web version of this article.)

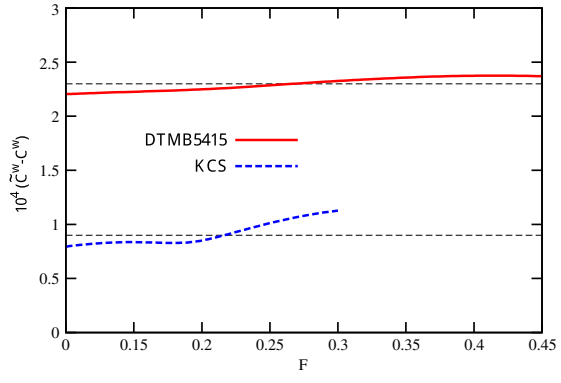

Fig. 3. Difference $\widetilde{C}^w - C^w$ between the linear wave drag $\widetilde{C}^w$ and the nonlinear wave drag C^w for the DTMB5415 and KCS ship models.

and KCS ship models. These nonlinear and linear approximations to the sinkage, the trim angle and the wave drag are determined via the relations (3)–(5), where the dynamic pressure p^* or the related linear approximation $\widetilde{p}^* = \phi_x$ given by (2) are used. Fig. 2 also depicts the sinkage H_a^m/L and the trim angle τ_a predicted by the explicit analytical relations (3), and experimental measurements of the sinkage H^m/L, the trim angle τ and the residuary drag C^r.

Differences between the nonlinear and linear predictions of the trim angle and the wave drag – except for the wave drags of the DTMB5415 and KCS models, considered further on – are small. Differences are somewhat larger, although not very large, for the sinkage. The small differences between nonlinear and linear predictions of the trim angle, the wave drag and (to a lesser extent) the midship sinkage, depicted in Fig. 2 mean that the contribution of the nonlinear component $|\nabla\phi|^2/2$ in expression (2a) for the dynamic pressure p^* is relatively small, except at the bulbs of the DTMB5415 and KCS models as is shown further on. Fig. 2 also shows that the sinkage H_a^m/L and the trim angle τ_a predicted by the explicit analytical relations (3) are in relatively good agreement with the numerical predictions.

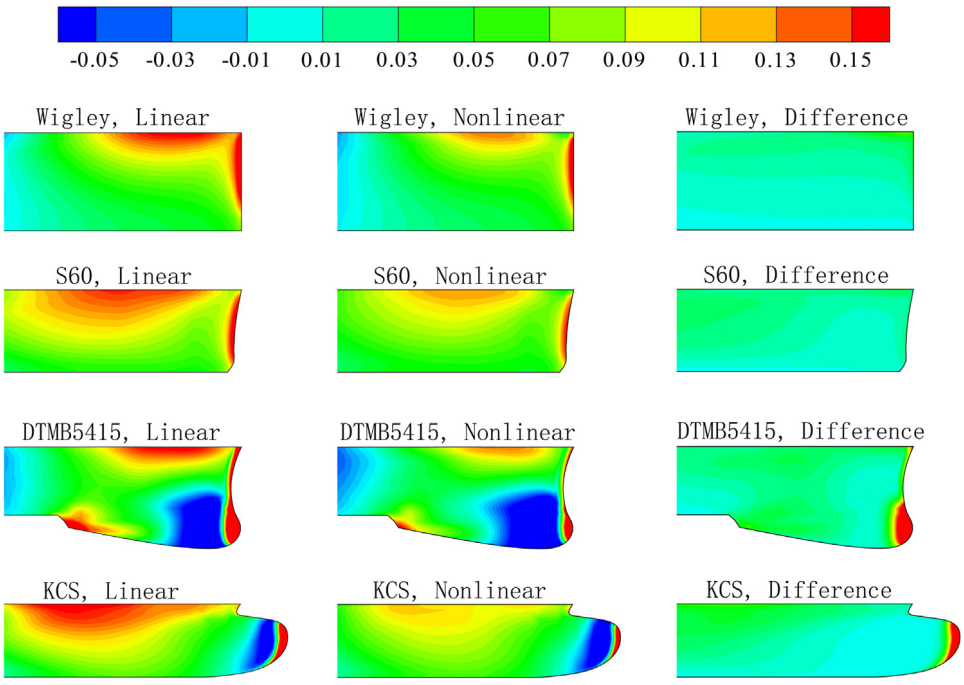

Fig. 4. Pressure distributions over the forebodies $0.35 \le x \le 0.5$ of the Wigley (top row), S60 (second row), DTMB5415 (third row) and KCS (bottom row) ship models. The left, center and right columns show the linearized pressure $\widetilde{p}^* = \phi_x$, the nonlinear pressure p^* and the difference $\widetilde{p}^* - p^*$.

However, differences between the linear and nonlinear predictions $\widetilde{C}^w$ and C^w of the wave drag are quite large for the DTMB5415 and KCS models, which have large bulbs as is shown in Fig. 1. Specifically, the linear drag $\widetilde{C}^w$ is much larger than the experimental measurements, whereas the nonlinear wave drag C^w and the measurements are relatively close. These large differences are easily explained, as is illustrated in Figs. 3 and 4 now considered.

Fig. 3 shows that the difference $\widetilde{C}^w - C^w$ between the linear and nonlinear predictions $\widetilde{C}^w$ and C^w is nearly independent of the Froude number F. The large differences between the linear and nonlinear predictions for the DTMB5415 and KCS models, and the fact that these differences do not vary much with speed, stem from the large bulbs of these two ship models. Indeed, the nonlinear and linear pressures are not very different over the wetted hull surfaces of the DTMB5415 and KCS models, except at the bulbs of the DTMB5415 and KCS models as is shown in Fig. 4.

Specifically, Fig. 4 depicts the linear pressure $\widetilde{p}^*$, the nonlinear pressure p^* and the difference $\widetilde{p}^* - p^*$ over the fore $0.35 \le x \le 0.5$ of the Wigley, S60, DTMB5415 and KCS models. The figure shows that differences between the linear and nonlinear pressures are relatively small everywhere except at the front of the bulbs of the DTMB5415 and KCS models, where $n^x \approx 1$ and stagnation points exist. Thus, Fig. 4 provides a particularly simple illustration of the effectiveness of bulbs for reducing the wave drag. The difference $\widetilde{C}^w - C^w$ between the linear and nonlinear wave drags is nearly independent of the Froude number, as is shown in Fig. 3, because no significant interferences occur between the large force associated with a high pressure over the forward faces of the large bulbs and the much smaller force associated with the pressure at the sterns for the DTMB5415 and KCS models.

The nonlinear theoretical predictions and the experimental measurements of sinkage and trim depicted in Fig. 2 are in very good agreement for the four ship models within the entire range of Froude numbers $0.1 \le F \le 0.45$ considered here. Fig. 2 also shows that the nonlinear wave drag C^w agrees well with the residuary drag C^r for the four ship models within the range of Froude numbers $0.25 \le F \le 0.45$.

4. Wave profile

4.1. Linear and nonlinear wave profiles

The Bernoulli relation (1a) defines the elevation $\zeta \equiv E/L$ or $\eta \equiv gE/V^2$ of the free surface, where $p = 0$, as

$$\eta \equiv \zeta/F^2 = p^*_{z=\zeta} \approx p^*_{z=0} + \zeta(\partial p^*/\partial z)_{z=0} + \cdots \tag{6a}$$

where the subscripts $_{z=\zeta}$ and $_{z=0}$ mean evaluation at the actual free surface $z = \zeta$ or at the undisturbed free surface $z = 0$. Inaccuracies associated with the numerical evaluation of the derivative $\partial p^*/\partial z$, which involves second derivatives of the velocity potential ϕ, are avoided if the (realistic) assumption that p^* varies exponentially in the vicinity of the free surface is made. The relation

$$p^* \approx p^*_{z=0}\, e^{k_e z} \tag{6b}$$

is then used here. The effective wavelength $\lambda_e \equiv 2\pi/k_e$ associated with the wavenumber k_e in (6b) is considered further on. The relations (6) yield

$$\eta \approx p^*_{z=0} + \zeta k_e\, p^*_{z=0} + \cdots = p^*_{z=0}\, e^{k_e \zeta}.$$

This relation and the identity $\zeta \equiv F^2\eta$ yield

$$\eta\, e^{-\sigma\eta} \approx p^*_{z=0} \tag{7a}$$

where

$$\sigma \equiv F^2 k_e = \frac{2\pi F^2}{\lambda_e} = \frac{\lambda_{max}}{\lambda_e}. \tag{7b}$$

Here, $\lambda_{max} \equiv 2\pi F^2$ is the wavelength of the longest waves created by a ship along its track. The relations (7) determine the free-surface elevation $\eta \equiv gE/V^2$ in terms of the hydrodynamic pressure $p^*_{z=0}$ and the effective wavelength λ_e. In particular, the wave profile along a ship hull, i.e. the free-surface elevation at the hull surface Σ^H, can be determined from Eq. (7a) where the pressure $p^*_{z=0}$ is evaluated via (2a)

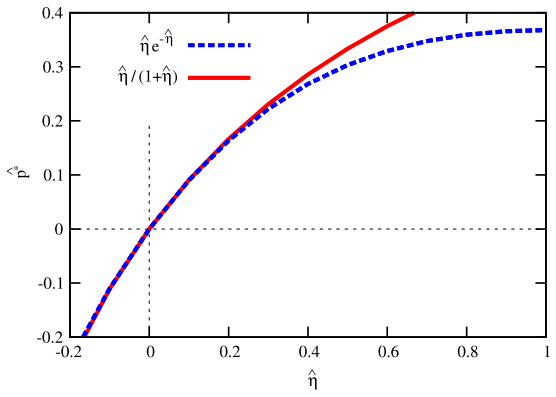

Fig. 5. Functions $\widehat{p^*} = \widehat{\eta}\, e^{-\widehat{\eta}}$ and $\widehat{p^*} = \widehat{\eta}/(1+\widehat{\eta})$ for $-0.2 \le \widehat{\eta} \le 1$.

The relation (7a) and the linear approximation $\widetilde{p^*} \approx \phi_x$ readily yield the linear approximation to the free-surface wave elevation

$$\widetilde{\eta} \approx \phi_x \tag{8a}$$

where ϕ_x is evaluated at the undisturbed free surface $z = 0$. The relation (7a) and the approximation $e^{\sigma\eta} \approx 1 + \sigma\eta$ yields the nonlinear correction

$$\eta \approx p^*/(1 - \sigma p^*) \tag{8b}$$

where p^* is evaluated at $z = 0$. Computations based on the NM theory show that the linear approximation (8a) and the nonlinear approximation (8b) do not differ significantly, and both approximations are in satisfactory agreement with the experimental measurements, for the four ship models considered here. However, these two approximations are markedly different from the approximation $\eta \approx p^*$, which definitely is not a good approximation.

More generally, the relation (7a) and the nonlinear approximation (8b) can be expressed as

$$\widehat{\eta}\, e^{-\widehat{\eta}} = \widehat{p^*} \tag{9a}$$

$$\widehat{\eta}/(1+\widehat{\eta}) = \widehat{p^*} \tag{9b}$$

$$\text{where} \quad \widehat{\eta} \equiv \sigma\eta \quad \text{and} \quad \widehat{p^*} \equiv \sigma p^*. \tag{9c}$$

The functions $\widehat{\eta}\, e^{-\widehat{\eta}}$ and $\widehat{\eta}/(1+\widehat{\eta})$, depicted in Fig. 5 for $-0.2 \le \widehat{\eta} \le 1$, do not differ very much within the range $-0.2 \le \widehat{\eta} \le 0.4$. Indeed, the wave profiles obtained via the alternative relations (9a) and (9b) are found to be nearly identical for $\sigma = 1$. Specifically, NM computations show that the approximation η_1 defined by the relation $\eta_1\, e^{-\eta_1} = p^*$, which corresponds to $\sigma = 1$ in (7a), is nearly indistinguishable from the approximation (8b), which is identical to (9b), for the four ship models considered here.

4.2. Effective wavelength

The relations (7) determine the wave profile, i.e. the elevation $\eta \equiv gE/V^2$ of the free surface along a ship hull, in terms of the hydrodynamic pressure $p^*_{z=0}$ and the effective wavelength λ_e of the waves at the ship waterline. Realistic choices for the effective wavelength λ_e are successively considered in this section for the waves aft of the bow wave and for the bow wave, which is shorter and higher than the waves aft of the bow wave.

The waves along the waterline of a ship, aft of the bow wave, approximately consist of plane waves with wavelength λ_{max}. Thus, the effective wavelength λ_e and the related parameter σ in (7a) are approximately given by $\lambda_e \approx \lambda_{max}$ and $\sigma \approx 1$ along the waterline aft of the bow wave. The nonlinear approximation η_1 defined by the relation $\eta_1\, e^{-\eta_1} = p^*$, which corresponds to $\sigma = 1$ in (7a) as was already noted, and the linear approximation $\widetilde{\eta} = \phi_x$ to the wave profiles for the Wigley, S60, DTMB5415 and KCS ship models are depicted in Fig. 6, where experimental measurements are also shown. Differences between the linear and nonlinear wave profiles $\widetilde{\eta}$ and η_1 are not very large. This result suggests that free-surface nonlinearities have a limited, although appreciable, influence on the wave profile. Moreover, the nonlinear approximation η_1 is not noticeably better than the linear approximation $\widetilde{\eta}$, and both approximations are in relatively good overall agreement with the experimental measurements.

However, a notable difference between the linear and nonlinear wave profiles depicted in Fig. 6 is that the linear approximation $\widetilde{\eta} = \phi_x$ predicts a higher bow wave, in better agreement with measurements, than the nonlinear approximation η_1 in all cases except the S60 model at low Froude numbers $F \le 0.26$, for which the two approximations predict nearly identical bow-wave heights. This seemingly surprising result stems from the assumption $\sigma \approx 1$, i.e. $\lambda_e \approx \lambda_{max}$, that is used in the nonlinear approximation η_1. In reality, the bow wave created by a ship is shorter (as well as higher and steeper) than the waves aft of the bow wave, as was already noted. At the bow wave, the parameter σ defined by (7b) can then be expected to be significantly larger than the value $\sigma = 1$ assumed in the approximation η_1 and in Fig. 6. A judicious choice for the effective wavelength λ_e of the bow wave in (7b) is then essential to obtain realistic predictions of ship bow waves, as well as for correctly filtering unrealistic short waves as is shown [4,7]. The choice of an effective bow-wave wavelength λ_e is now considered, based on the theoretical considerations given in [1,4] and an analysis of experimental measurements of wave profiles for the Wigley, S60 and DTMB5415 models.

Three reasonable alternative estimates of the effective wavelength λ_e of a ship bow wave are

$$\lambda_0 \approx 2(0.5 - x_0), \qquad \lambda_{0b} \approx 4(x_b - x_0) \tag{10a}$$

$$\lambda_b \approx 4(0.5 - x_b) \equiv 2\lambda_0 - \lambda_{0b}. \tag{10b}$$

Here, $x_b \equiv X_b/L$ and $x_0 \equiv X_0/L$ denote the x-coordinates of the crest of the bow wave and the intersection of the bow-wave profile with the undisturbed free surface $z = 0$, as is shown in Fig. 7. The relations (10) and (7b) yield the estimates

$$\sigma_0 \approx \frac{\pi F^2}{0.5 - x_0}, \qquad \sigma_0^b \approx \frac{\pi F^2/2}{x_b - x_0} \tag{11a}$$

$$\sigma_b \approx \frac{\pi F^2/2}{0.5 - x_b} \equiv \frac{\sigma_0}{2 - \sigma_0/\sigma_0^b} \tag{11b}$$

of the parameter σ in (7a). The effective-wavelength parameters σ_0, σ_0^b and σ_b are depicted in Fig. 8 for the Wigley, S60 and DTMB5415 ship models. This figure shows that the alternative

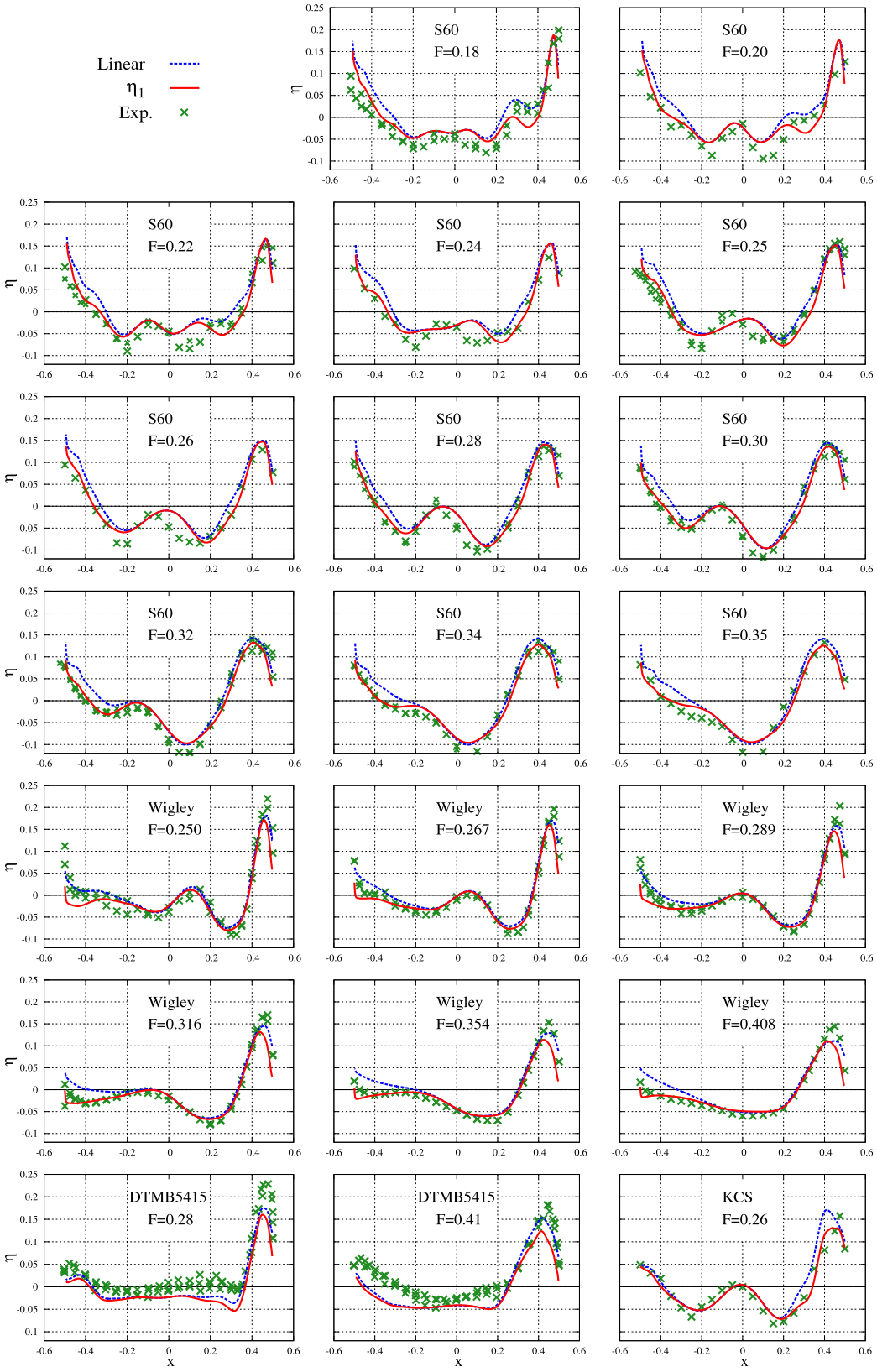

Fig. 6. Linear approximation $\widetilde{\eta} = \phi_x$ and nonlinear approximation η_1 defined by the relation $\eta_1\, e^{-\eta_1} = p^*$, which corresponds to $\sigma = 1$ in (7a), to the wave profiles for the Wigley, S60, DTMB5415 and KCS ship models. Experimental measurements are also shown.

estimates (11) of the parameter σ associated with the effective wavelength λ_e of a ship bow wave are mostly and significantly greater than 1, with the exception of σ_0^b for the S60 model at $F \le 0.26$. Fig. 8 also shows that one has $\sigma_0^b < \sigma_0 < \sigma_b$, in accordance with the fact that the front of a ship bow wave is shorter than the back of the wave. In particular, (11a) yields

$$1 \le \sigma_0 \quad \text{if } \frac{0.5 - x_0}{F^2} \equiv \frac{(L/2 - X_0)g}{V^2} \le \pi\,. \tag{12}$$

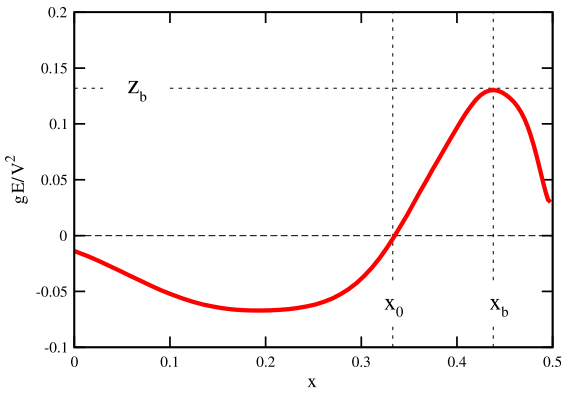

Fig. 7. Locations $x_b \equiv X_b/L$ and $x_0 \equiv X_0/L$ of the crest of a ship bow wave and of the intersection of the bow-wave profile with the undisturbed free surface $z = 0$.

Moreover, Fig. 8 shows that σ_0, σ_0^b and σ_b increase with F. Indeed, the analysis of ship bow waves considered in [1,34,35] shows that a ship bow wave can be approximately scaled according to the rule

$$(1 + F_d)\frac{\mathbf{X}g}{V^2} \quad \text{where } F_d \equiv \frac{V}{\sqrt{gD}} = F\sqrt{\frac{L}{D}} \tag{13}$$

denotes the Froude number based on the draft D of the ship. In particular, the scaling law (13) means that the basic features

$$\frac{1 + F_d}{F^2}[0.5 - x_0, 2(x_b - x_0), 2(0.5 - x_b), z_b] = [C_0, C_0^b, C_b, C_b^z] \tag{14}$$

of a ship bow wave, where $z_b \equiv Z_b/L$ denotes the height of the bow wave as is shown in Fig. 7, can be expected to be nearly independent of the Froude number F, i.e. to be equal to constants. These constant values are denoted as C_0, C_0^b, C_b and C_b^z in (14). The scaling law (14) is validated in Fig. 9 for the Wigley, S60 and DTMB5415 ship models.

The relations (11) and (14) yield

$$\frac{[\sigma_0, \sigma_0^b, \sigma_b]}{1 + F_d} \approx \left[\frac{\pi}{C_0}, \frac{\pi}{C_0^b}, \frac{\pi}{C_b}\right]. \tag{15}$$

These relations and the average values of C_0, C_0^b and C_b for the Wigley, S60 and DTMB5415 models noted in Fig. 9 yield

$$[\sigma_0^b, \sigma_0, \sigma_b]/(1 + F_d) \approx$$

$$[0.42, 0.58, 0.92] \quad \text{for the S60 model} \tag{16a}$$

$$[0.58, 0.73, 0.98] \quad \text{for the DTMB5415 model} \tag{16b}$$

$$[0.71, 0.85, 1.05] \quad \text{for the Wigley model.} \tag{16c}$$

The effective wavelength parameter σ_0 does not differ very much from the average $(\sigma_0^b + \sigma_0 + \sigma^b)/3$, equal to 0.64, 0.76, 0.87 for the S60, DTMB5415 and Wigley models. The values of σ_0^b, σ_0 and σ_b listed in (16) also show that $\sigma_0^b < \sigma_0 < \sigma_b$ as was already noted. Moreover, (16) shows that the alternative effective wavelength parameters σ_0^b, σ_0 and σ_b are consistently smallest for the S60 model and highest for the Wigley model. This result means that the effective wavelength is longest for the S60 model and shortest for the Wigley hull, and suggests that nonlinearities might be weakest for the S60 model and strongest for the Wigley hull.

The bow-wave scaling law (13) is further illustrated in Fig. 10. Specifically, this figure depicts experimental measurements and NM linear predictions $\widetilde{\eta}$ of bow-wave profiles in accordance with the scaling relations

$$(1 + F_d)Eg/V^2 \quad \text{and} \tag{17a}$$

$$\xi \equiv (1 + F_d)(X - L/2)g/V^2 \tag{17b}$$

for $-6 \le \xi \le 0$. Both the experimental measurements and the NM linear predictions for the Wigley, S60 and DTMB5415 ship models, at six, eleven or two Froude numbers, approximately coalesce in Fig. 10, in agreement with the relations (17). Indeed, these scaling relations are shown in [1,34,35] to be approximately valid for ship bow waves, except at the stem of a ship where the rise of water follows a different scaling law [36]. Fig. 10 also shows that the NM linear bow-wave profiles are in relatively good overall agreement with the experimental measurements, as was already observed in Fig. 6. In particular, the figure shows that the bow-wave height predicted by the NM linear theory is slightly higher than the experimental bow-wave height for the S60 model but slightly lower for the Wigley and S60 models. Fig. 10 also shows that the experimental measurements and the theoretical predictions, separated into three groups that correspond to Froude numbers F within the ranges $F < 0.25$, $0.25 < F < 0.3$ and $0.3 < F$, are largely found above or below the polynomial fits of all the experimental measurements and the theoretical predictions in a fairly consistent manner for the Wigley and S60 models (for which wave profiles are shown for six or eleven Froude numbers). This finding suggests that the scaling law (17) is not perfect and could perhaps be refined. E.g. the draft D used to define the Froude number F_d might be replaced by an effective draft D_e that depends on the Froude number F.

The influence of nonlinearities is illustrated in Fig. 11 via comparisons of the linear bow-wave profile $\widetilde{\eta} = \phi_x$, the pressure $p^*_{z=0}$, and the nonlinear profile η_1 associated with the simplest choice $\sigma = 1$ in (7a) and already considered in Fig. 6. Fig. 11 shows that the pressure $p^*_{z=0}$ is consistently smaller than the linear profile $\widetilde{\eta} = \phi_x$ in accordance with (1b). Differences between $\widetilde{\eta}$ and $p^*_{z=0}$ are appreciable, although not very large. The nonlinear bow-wave profile η_1 also lies below the linear profile $\widetilde{\eta}$, but is closer to the linear profile $\widetilde{\eta}$ than the pressure $p^*_{z=0}$. The bottom row of Fig. 11 shows that, except for the S60 model, the linear bow-wave profile $\widetilde{\eta}$ is closer to the experimental profile than the nonlinear profile η_1, as was already noted in Fig. 6.

Fig. 12 depicts measurements of wave profiles for the Wigley, S60 and DTMB5415 models for the range $-30 \le \xi \le 0$ instead of the narrower range $-6 \le \xi \le 0$ already considered in Fig. 10. Fig. 12 shows that the scaling law (17) does not hold for the entire wave profile (although the wave profiles for the Wigley hull approximately coalesce for the relatively wide range $-15 \le \xi \le 0$), i.e. is a 'bow-wave scaling law' that only applies to bow waves.

4.3. Practical nonlinear correction of linear wave profile

As was already noted, Fig. 6 shows that the bow wave predicted by the nonlinear approximation η_1, which corresponds to $\sigma = 1$ in (7a), is lower and in poorer agreement with measurements than the bow wave predicted by the linear approximation $\widetilde{\eta} = \phi_x$. Moreover, the foregoing analysis of ship bow waves suggests that nonlinear bow waves that better agree with measurements may be expected if a realistic effective-wavelength parameter $\sigma \equiv \lambda_{max}/\lambda_e$ is used in (7a).

The effective-wavelength parameter σ in (7a) can be estimated from experimental measurements η^{exp} of wave profiles and NM predictions of the pressure $p^*_{z=0}$ via the relation (7a). Specifically, this relation yields

$$\sigma_{NM}^{exp} = \frac{1}{\eta^{exp}} \ln \frac{\eta^{exp}}{p^*_{z=0}}. \tag{18}$$

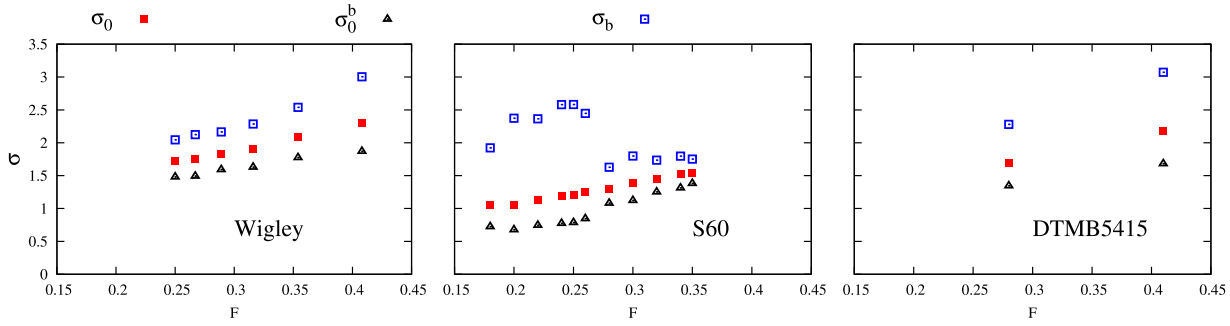

Fig. 8. Effective-wavelength parameters σ_0, σ_0^b and σ_b defined by (11) for the Wigley, S60 and DTMB5415 models. These parameters are determined from the nonlinear approximation η_1 predicted by the NM theory and depicted in Fig. 6.

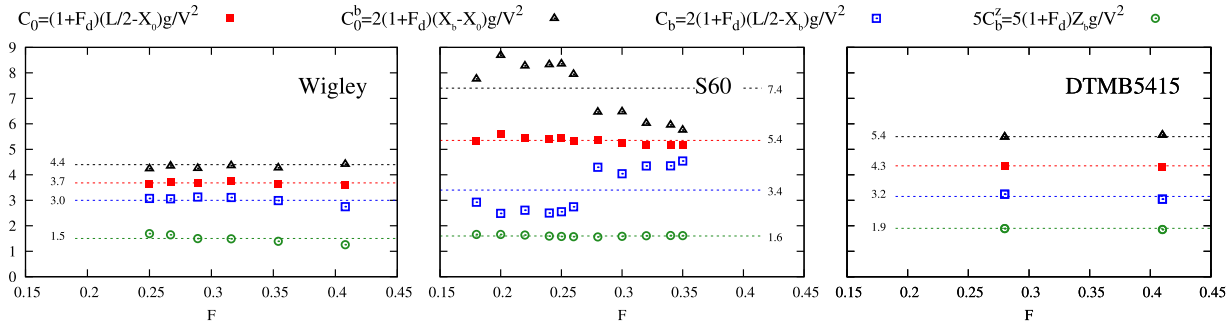

Fig. 9. Values of $(1+F_d)(L/2-X_0)\,g/V^2$, $2(1+F_d)(X_b-X_0)\,g/V^2$, $2(1+F_d)(L/2-X_b)\,g/V^2$ and $5(1+F_d)Z_b\,g/V^2$ for the Wigley, S60 and DTMB5415 ship models. The dashed horizontal lines represent averages of the values for the Froude numbers considered in the figure.

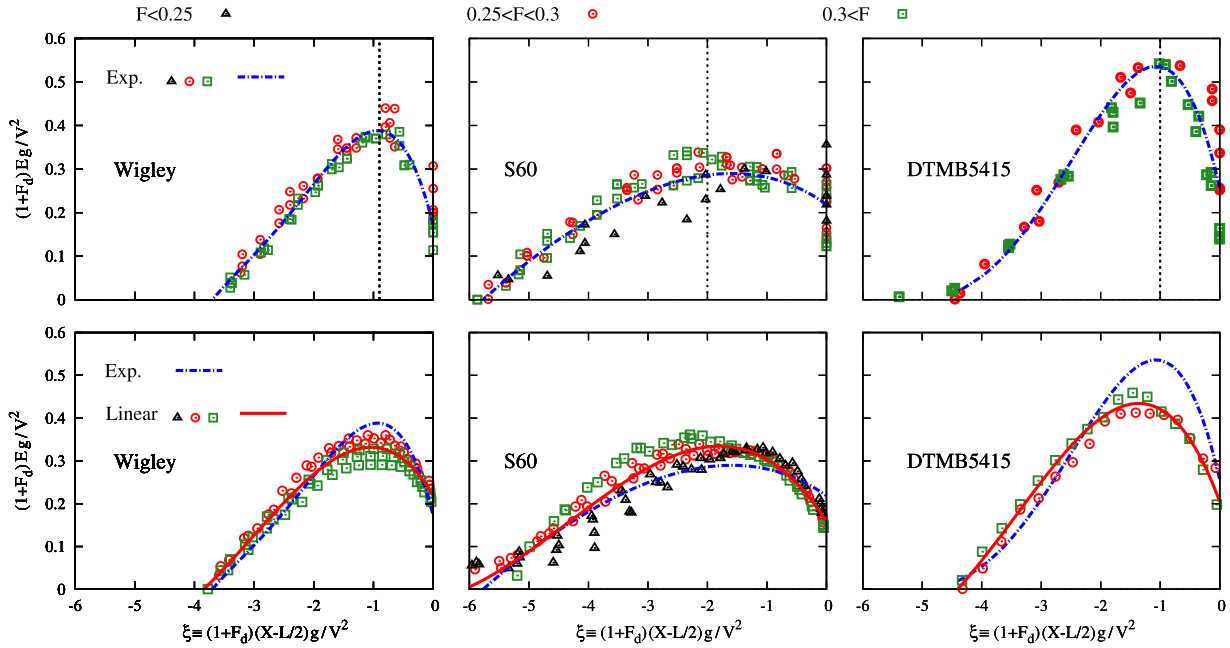

Fig. 10. Experimental measurements (top row) and NM-theory linear predictions $\widetilde{\eta}$ (bottom row) of the bow-wave profiles $(1+F_d)Eg/V^2$ for the Wigley (left column), S60 (center column) and DTMB5415 (right column) ship models and $-6 \le (1+F_d)(X-L/2)g/V^2 \le 0$. The dashed blue lines in the top row and the solid red lines in the bottom row correspond to average values of the experimental measurements or the linear NM predictions η_1. (For interpretation of the references to color in this figure legend, the reader is referred to the web version of this article.)

The effective-wavelength parameter σ_{NM}^{exp} determined via (18) from experimental measurements and NM theoretical predictions for the Wigley, S60 and DTMB5415 models is depicted in Fig. 13 for $-3 \le \xi \le 0$. The figure also shows the three alternative effective-wavelength parameters σ_0^b, σ_0, σ_b given by (16), and polynomial fits of σ_{NM}^{exp}. Moreover, the locations ξ_b of the bow wave crests – given by $\xi_b \approx -0.9, -2, -1$ for the Wigley, S60, DTMB5415 models – are marked as vertical lines in Fig. 13. The figure shows that (despite considerable scatter, notably for $\xi < -2$) the values of σ_{NM}^{exp} determined from experimental measurements and NM predictions increase as $\xi \to 0$, i.e. are larger in the vicinity of the ship stem $\xi = 0$, as is expected. Indeed, the front of a ship bow wave is much steeper than the back of the wave, and is approximately parabolic [1]. Fig. 13 also shows that the values of

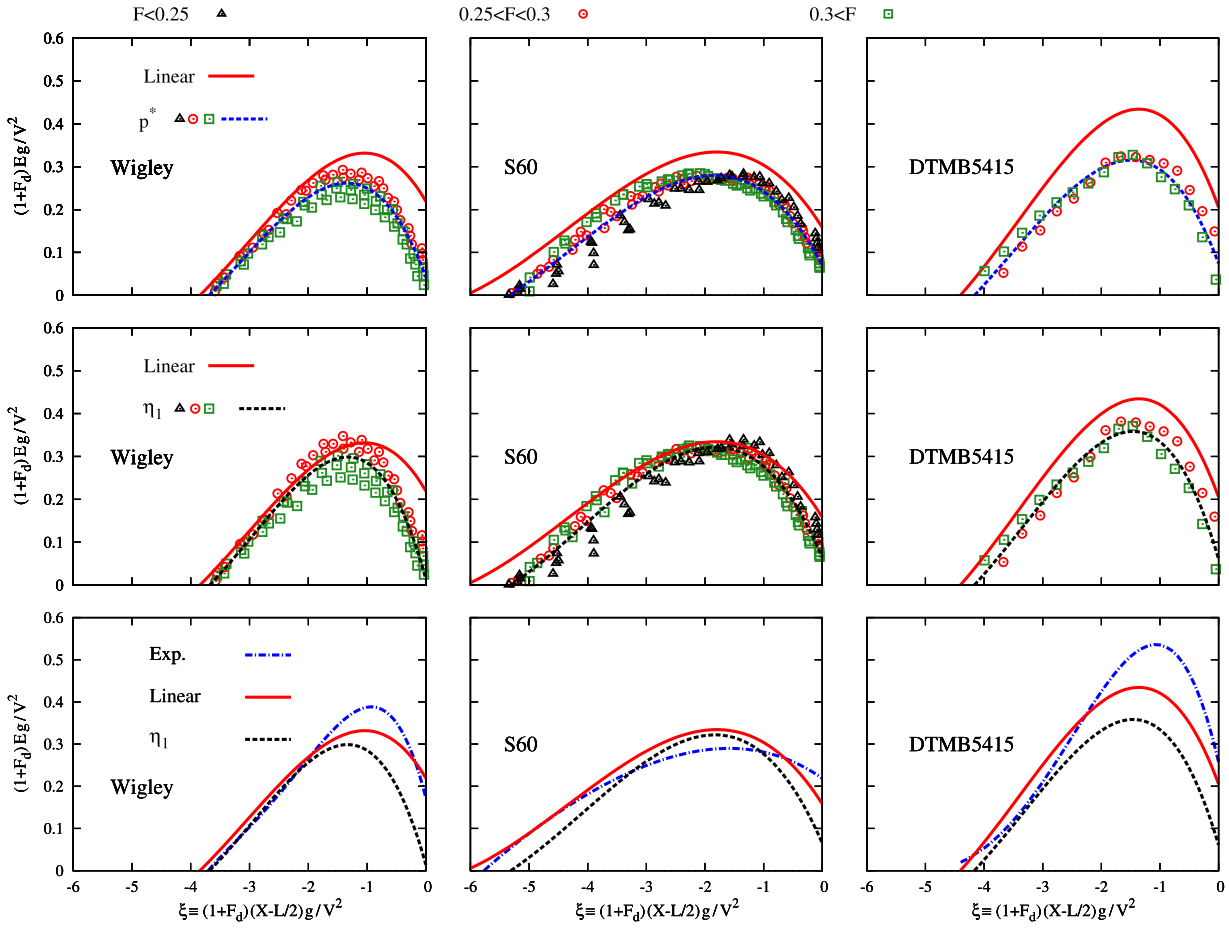

Fig. 11. NM linear profile $\widetilde{\eta}$, pressure $p^*_{z=0}$, nonlinear profile η_1 and experimental measurements of the scaled bow-wave profiles $(1+F_d)Eg/V^2$ of the Wigley (left column), S60 (center column) and DTMB5415 (right column) models for $-6 \le (1+F_d)(X-L/2)g/V^2 \le 0$. The dashed blue lines in the top row and the dashed black lines in the center row correspond to average values of $p^*_{z=0}$ (top) or η_1 (bottom). (For interpretation of the references to color in this figure legend, the reader is referred to the web version of this article.)

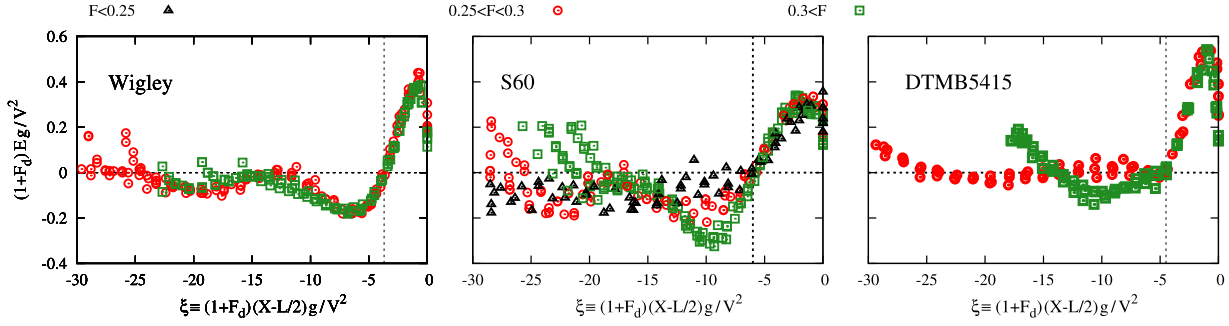

Fig. 12. Experimental wave profiles $(1+F_d)Eg/V^2$ of the Wigley (left), S60 (center) and DTMB5415 (right) models for $-30 \le (1+F_d)(X-L/2)g/V^2 \le 0$. This figure shows that the bow-wave scaling law illustrated in Figs. 10 and 11 does not hold for the entire wave profile.

σ^{exp}_{NM} in the vicinity of the location ξ_b of the crest of the bow wave are consistent with the values of the alternative parameters σ^b_0, σ_0, σ_b given by (16).

Fig. 14 depicts the ratio $\sigma^{exp}_{NM}/\sigma_0$ of the effective-wavelength parameters σ^{exp}_{NM} and σ_0 already considered in Fig. 13. The vertical lines $\xi_b \approx -0.9, -2, -1$ in Fig. 14 correspond to the locations of the bow wave crests for the Wigley, S60, DTMB5415 models, as in Fig. 13. Fig. 14 shows that, although considerable scatter can be observed among the data, the ratio $\sigma^{exp}_{NM}/\sigma_0$ may reasonably be assumed to be approximately independent of the hull shape and the Froude number F, and can be roughly approximated as

$$\sigma/\sigma_0 = 0.5 + 0.78/(0.12 - \xi) \tag{19a}$$

where $\xi \le 0$ is given by (17b). Moreover, σ_0 is defined by (11a) as

$$\sigma_0 = \pi F^2/(0.5 - x_0) \tag{19b}$$

where $x_0 \equiv X_0/L$ is now taken as the x-coordinate of the first intersection of the pressure $p^*_{z=0}$ with the undisturbed free surface $z = 0$.

The relation (7a), where the effective-wavelength parameter σ is determined via (19), provides a simple method for constructing a nonlinear wave profile η from the pressure $p^*_{z=0}$ predicted by the linear NM theory. The nonlinear correction of the NM linear wave profile defined by the relations (7a) and (19) is an elementary (post-processing) procedure that requires no additional flow

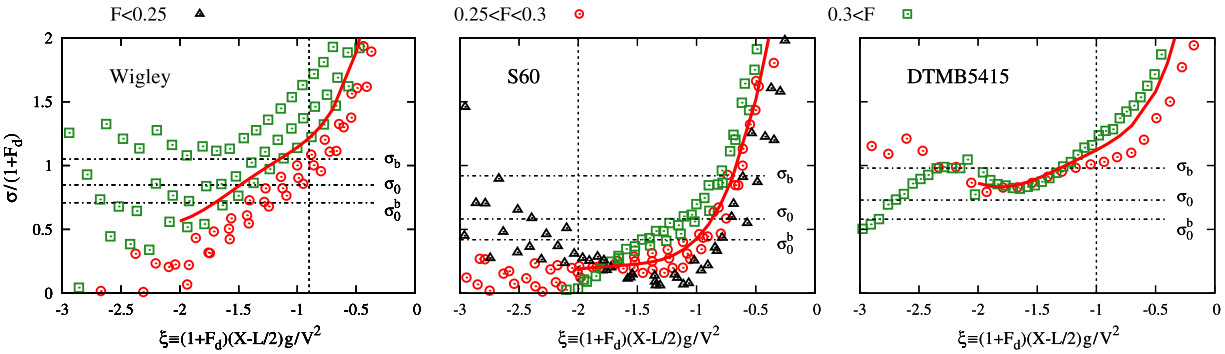

Fig. 13. Values of the effective-wavelength parameter σ_{NM}^{exp} determined via (18) for the Wigley (left), S60 (center) and DTMB5415 (right) models; the red solid lines correspond to average values for $-2 \le (1+F_d)(X-L/2)g/V^2$. The three dashed horizontal lines correspond to the three alternative effective-wavelength parameters σ_0^b, σ_0 and σ_b given by (16) and depicted in Fig. 9. (For interpretation of the references to color in this figure legend, the reader is referred to the web version of this article.)

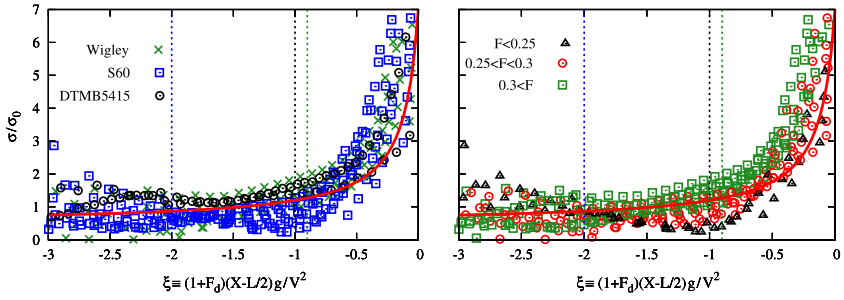

Fig. 14. Values of the parameter $\sigma_{NM}^{exp}/\sigma_0$ determined from (18) and the intersection x_0 of the bow-wave profile with the mean free surface $z = 0$. The related fit (19) is depicted as solid red lines. (For interpretation of the references to color in this figure legend, the reader is referred to the web version of this article.)

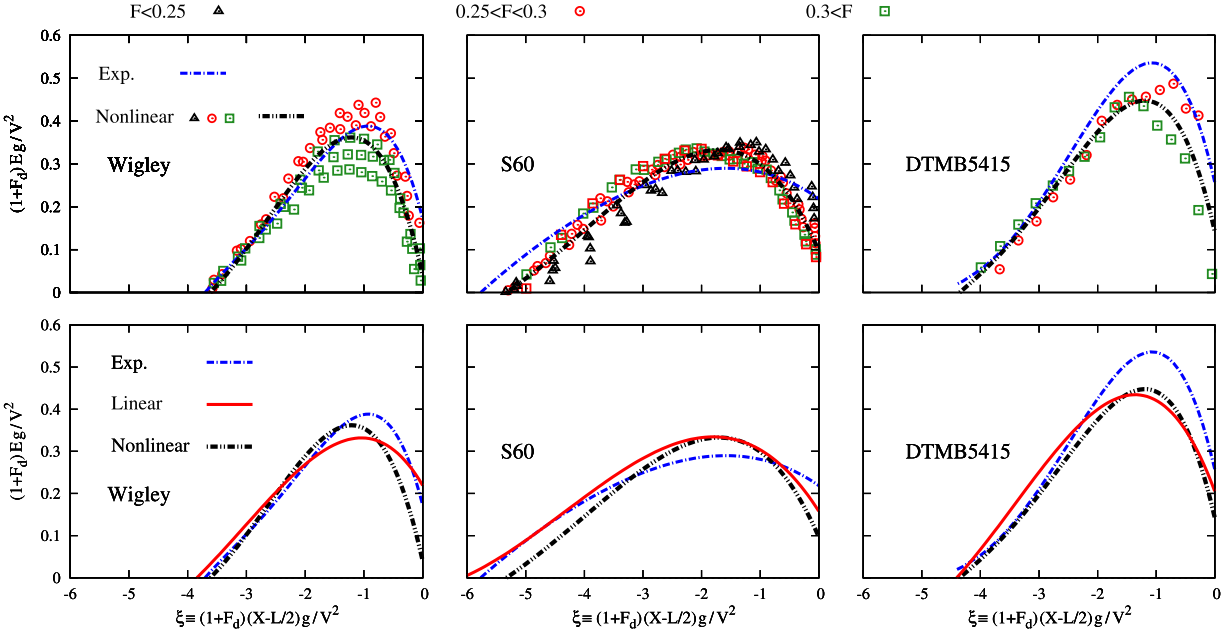

Fig. 15. Nonlinear bow-wave profiles determined from (7a), where the effective-wavelength parameter σ is given by (19), linear profiles $\widetilde{\eta} = \phi_x$ and experimental measurements for the Wigley (left column), S60 (center column) and DTMB5415 (right column) models.

computations. Although the scatter among the values of the ratio $\sigma_{NM}^{exp}/\sigma_0$ depicted in Fig. 14 shows that the nonlinear correction defined by (7a) and (19) cannot be expected to be accurate, comparison of the NM linear wave profile $\widetilde{\eta}$ and the related nonlinear profile η determined via (7a) and (19) provides an estimate of the influence of nonlinearities on the wave profile. This estimate is sufficient in many practical cases because differences between the linear and nonlinear wave profiles are not very large, and are largely inconsequential for typical practical applications.

The nonlinear bow-wave profile η determined from linear NM flow computations via (7a) and (19), and the corresponding linear profile $\widetilde{\eta}$ and experimental measurements, are depicted in Fig. 15 for the Wigley, S60 and DTMB5415 ship models at six, eleven

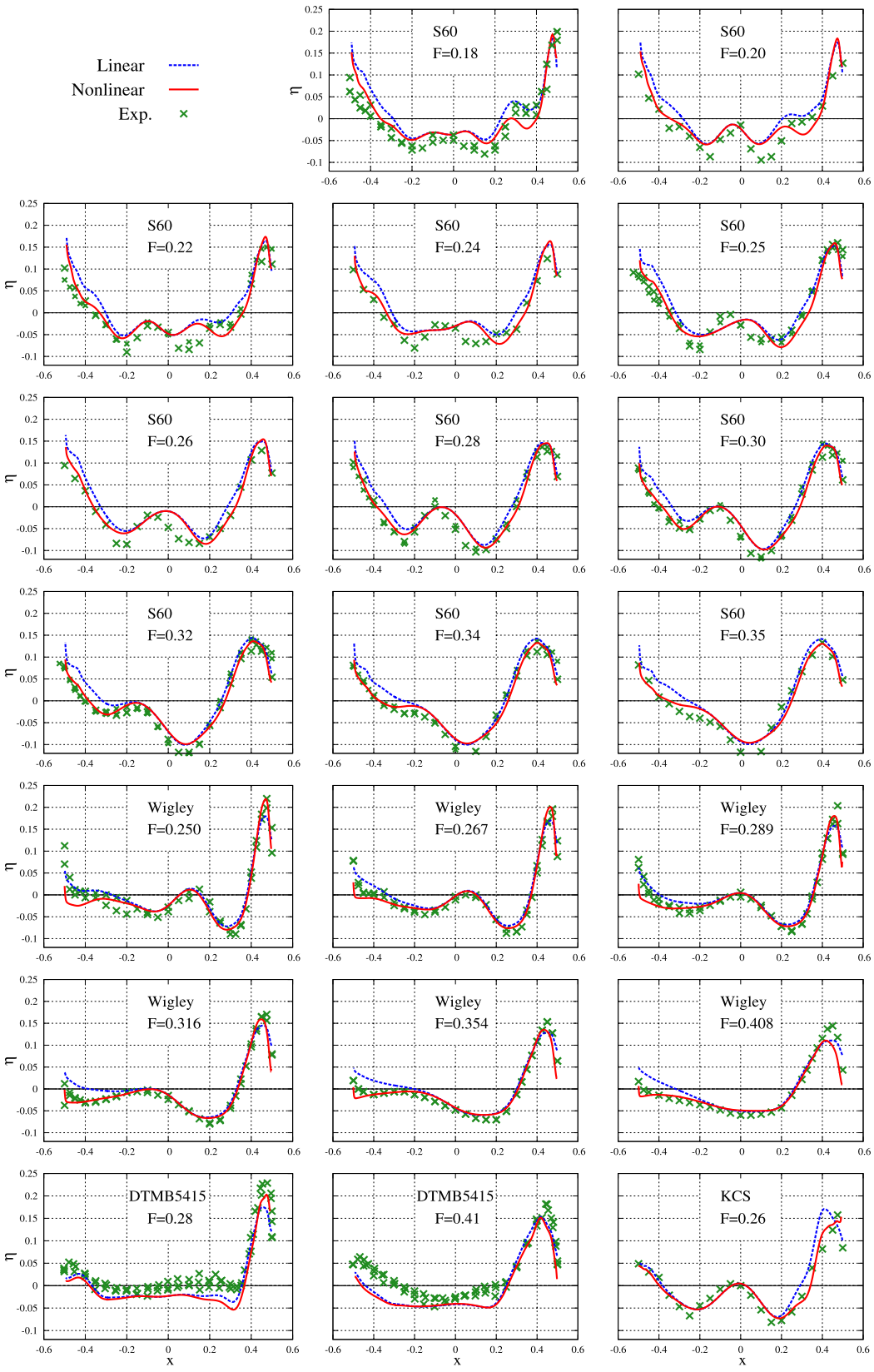

Fig. 16. Experimental measurements, linear wave profiles $\widetilde{\eta} = \phi_x$ and nonlinear profiles determined from (7a), where the effective-wavelength parameter σ is given by (19), for the Wigley, S60, DTMB5415 and KCS models.

or two Froude numbers. This figure shows that differences between the linear and nonlinear bow-wave profiles $\widetilde{\eta}$ and η are appreciable, although not very large. The nonlinear bow wave is slightly higher and noticeably sharper than the linear bow wave, and qualitatively in better agreement with the experimental bow wave, for the Wigley and DTMB5415 models. However, the linear

bow wave is somewhat closer to the experimental bow wave than the nonlinear bow wave for the S60 model, for which nonlinearities appear to be weaker than for the Wigley and DTMB5415 models.

The linear and nonlinear wave profiles are depicted, together with experimental measurements, in Fig. 16 within the range $-0.5 \leq x \leq 0.5$ for the Wigley, S60, DTMB5415 and KCS ship models. Fig. 16 shows that the nonlinear wave profiles determined via the simple post-processing correction used here are in somewhat better agreement with the experimental measurements on the whole, although differences between the linear and nonlinear wave profiles are not very large. Indeed, both wave profiles are in satisfactory overall agreement with the experimental profiles.

5. Conclusions

Integration of the dynamic pressure $p^* \equiv \phi_x - |\nabla\phi|^2/2$, where the flow velocity $\nabla\phi \equiv (\phi_x, \phi_y, \phi_z)$ is determined via the NM (Neumann-Michell) linear potential flow theory, over the mean wetted hull surfaces of the (freely-floating) Wigley, S60, DTMB 5415 and KCS ship models at Froude numbers $F < 0.45$ yields predictions of the sinkage, the trim angle and the wave drag that are in satisfactory agreement with experimental measurements. Indeed, the nonlinear theoretical predictions and the experimental measurements of sinkage and trim depicted in Fig. 2 are in very good agreement for the four ship models within the entire range of Froude numbers $0.1 \leq F \leq 0.45$ considered here. Fig. 2 also shows that the nonlinear wave drag C^w agrees well with the residuary drag C^r for the four ship models within the range of Froude numbers $0.25 \leq F \leq 0.45$.

The nonlinear pressure component $|\nabla\phi|^2/2$ has a very small influence on the trim angle and an appreciable but relatively small effect on the sinkage for the four ship models considered here, and moreover also has a small influence on the wave drag for the Wigley and S60 hulls. These results suggest that nonlinear effects are relatively small. However, an important exception to this general finding is the wave drag of bulbous ships. Indeed, the nonlinear component $|\nabla\phi|^2/2$ has a very large effect on the wave drag of the DTMB5415 and KCS models, which have large bulbs, and this pressure component must be included to obtain realistic theoretical predictions of the wave drag.

The large differences between the linear and nonlinear predictions of the wave drag for the DTMB5415 and KCS models, and the fact that these differences do not vary much with speed, stem from the bulbs of these two ship models, as is demonstrated in Fig. 4. Specifically, this figure shows that differences between the linear and nonlinear pressures are relatively small everywhere except at the front of the bulb, where $n^x \approx 1$ and a stagnation point exists. The differences between the linear and nonlinear wave drags for the DTMB5415 and KCS models are nearly independent of the Froude number, as is shown in Fig. 3, because no significant interferences occur between the high pressures over the forward faces of the bulbs and the much smaller pressures at the sterns of the DTMB5415 and KCS models. Indeed, Fig. 4 provides a particularly simple illustration of the effectiveness of bulbs for reducing the wave drag.

The linear wave profile predicted by the NM theory can readily be modified – without additional flow computations – via a simple correction that approximately accounts for free-surface nonlinearities. The bow wave associated with the nonlinear wave profile that is constructed from linear NM flow computations via this simple correction – based on the Bernoulli relation, the assumption that the flow associated with the waves along a ship hull surface decays exponentially with depth, and an estimate (obtained via basic theoretical considerations and an analysis of experimental measurements) of the effective wavelengths of these waves – is somewhat closer to experimental measurements than the linear bow wave. However, differences between the linear wave profile given by the NM theory and the corresponding nonlinear profile are relatively small overall, and indeed both the linear and the nonlinear profiles are in satisfactory agreement with the experimental profiles. This finding suggests that the influence of free-surface nonlinearities on wave profiles is relatively small.

Indeed, the results of the analysis of nonlinear effects reported in the study do not support the view, largely expressed in the literature, that nonlinearities associated with the boundary condition at the free surface are an essential feature of the flow around a ship hull in calm water, and that a major limitation of linear potential flow theory is its inability to account for these nonlinearities. On the contrary, the analysis reported here provides evidence that free-surface nonlinearities are of limited importance, and indeed are largely inconsequential for most practical purposes, except for the influence of the nonlinear pressure component $|\nabla\phi|^2/2$ on the wave drag of a bulbous ship. This important nonlinear effect can readily be included within the NM linear theory. Moreover, the linear wave profiles predicted by the NM theory are easily modified to approximately account for free-surface nonlinearities, and the resulting nonlinear wave profiles compare favorably with the wave profiles predicted by alternative numerical methods.

The linear NM theory can also effectively account for the (large) influence of sinkage and trim on the drag of a freely-floating monohull ship, as is shown in [5,14]. A sequel to these previous studies of sinkage and trim effects on the drag and the present study of nonlinear effects will further extend the NM linear potential flow theory to account for viscous effects, notably for full-scale ships with rough hulls, on the wave drag. Indeed, a practical and realistic theory – that is robust, highly efficient, and accounts for all dominant flow physics – is required for routine applications to design and hydrodynamic optimization.

References

[1] F. Noblesse, G. Delhommeau, M. Guilbaud, D. Hendrix, C. Yang, Simple analytical relations for ship bow waves, J. Fluid Mech. 600 (2008) 105–132.

[2] G. Delhommeau, M. Guilbaud, L. David, C. Yang, F. Noblesse, Boundary between unsteady and overturning bow wave regimes, J. Fluid Mech. 620 (2009) 167–175.

[3] F. Noblesse, F. Huang, C. Yang, The Neumann-Michell theory of ship waves, J. Engrg. Math. 79 (1) (2013) 51–71.

[4] F. Huang, C. Yang, F. Noblesse, Numerical implementation and validation of the Neumann-Michell theory of ship waves, Eur. J. Mech. B Fluids 42 (2013) 47–68.

[5] C. Ma, C. Zhang, X. Chen, Y. Jiang, F. Noblesse, Practical estimation of sinkage and trim for common generic monohull ships, Ocean Eng. 126 (2016) 203–216.

[6] F. Noblesse, G. Delhommeau, F. Huang, C. Yang, Practical mathematical representation of the flow due to a distribution of sources on a steadily-advancing ship hull, J. Eng. Math. 71 (2011) 367–392.

[7] F. Noblesse, F. Huang, C. Yang, Evaluation of ship waves at the free surface and removal of short waves, Eur. J. Mech. B Fluids 38 (2013) 22–37.

[8] C. Zhang, J. He, Y. Zhu, W. Li, F. Noblesse, F. Huang, C. Yang, Stationary phase and numerical evaluation of farfield and nearfield ship waves, Eur. J. Mech. B/Fluids 52 (2015) 28–37.

[9] H. Wu, C. Zhang, C. Ma, F. Huang, C. Yang, F. Noblesse, Errors due to a practical Green function for steady ship waves, Eur. J. Mech. B Fluids 55 (2016) 162–169.

[10] C. Yang, F. Huang, F. Noblesse, Practical evaluation of the drag of a ship for design and optimization, J. Hydrodyn. Ser. B 25 (5) (2013) 645–654.

[11] F. Huang, X. Li, F. Noblesse, C. Yang, W. Duan, Illustrative applications of the Neumann-Michell theory of ship waves, in: 28th Il Workshop on Water Waves & Floating Bodies, L'Isle sur la Sorgue, France, 2013.

[12] C. Zhang, F. Noblesse, D. Wan, F. Huang, C. Yang, Partial validation and verification of the Neumann-Michell theory of ship waves, in: 11th Il Conf. Hydrodynamics, Singapore, 2014.

[13] C. Zhang, J. He, C. Ma, F. Noblesse, D. Wan, F. Huang, C. Yang, Validation of the Neumann-Michell theory for two catamarans, in: 25th Il Ocean & Polar Eng. Conf., ISOPE, Kona, Hawaii USA, 2015.

[14] C. Ma, C. Zhang, F. Huang, C. Yang, X. Gu, W. Li, F. Noblesse, Practical evaluation of sinkage and trim effects on the drag of a common generic freely floating monohull ship, Appl. Ocean Res. 65 (2017) 1–11.

[15] F. Huang, L. Wang, C. Yang, A new improved artificial bee colony algorithm for ship hull form optimization, Eng. Optim. 48 (4) (2016) 672–686.

[16] C. Yang, F. Huang, H. Kim, Hydrodynamic optimization of a TriSWACH, J. Hydrodyn. Ser. B 26 (6) (2014) 856–864.
[17] F. Huang, L. Wang, C. Yang, R. Royce, Hull form optimization of a TriSWACH for reduced drag, in: 13th Int. Conf. Fast Sea Transp., Washington DC, USA, 2015.
[18] L. Wang, F. Huang, C. Yang, R. Datla, Hydrodynamic optimization of a wedge hull, in: 13th Int. Conf. Fast Sea Transp., Washington DC, USA, 2015.
[19] C. Yang, F. Huang, L. Wang, A NURBS-based modification technique for bulbous bow generation and hydrodynamic optimization, in: 31st Symp. Nav. Hydrodyn., Monterey, California, USA (2016) 11–16.
[20] F. Huang, H. Kim, C. Yang, A new method for ship bulbous bow generation and modification, in: Twenty-Fourth Int. Ocean Polar Eng. Conf., International Society of Offshore and Polar Engineers, Busan, Korea, 2014.
[21] F. Huang, L. Wang, C. Yang, Hull form optimization for reduced drag and improved seakeeping using a surrogate-based method, in: The Twenty-Fifth Int. Ocean Polar Eng. Conf., International Society of Offshore and Polar Engineers, Kona, Hawaii, USA, 2015.
[22] F. Huang, C. Yang, Hull form optimization of a cargo ship for reduced drag, J. Hydrodyn. Ser. B 28 (2) (2016) 173–183.
[23] C. Yang, F. Huang, An overview of simulation based hydrodynamic design of ship hull forms, in: The Second Conference of Global Chinese Scholars on Hydrodynamics, Wuxi, China, 2016.
[24] H. Kajitani, H. Miyata, M. Ikehata, H. Tanaka, H. Adachi, The Summary of the Cooperative Experiment on the Wigley Parabolic Model in Japan, Tokyo Univ., Japan, 1983.
[25] Resistance Committee, Experimental data for the Wigley hull reported in cooperative experiments on the Wigley parabolic model in Japan, 17th ITTC Resistance Committee, Tech. Rep. 1983.
[26] H. Fuxin, A practical computational method for steady flow about a ship. Ph.D. thesis, George Mason University, 2013.
[27] Resistance Committee Experimental data for the series 60 model are reported in cooperative experiments on the series 60 ($C_b = 0.6$) model, 18th ITTC Resistance Committee, Tech. Rep. 1986.
[28] H. Takashi, T. Hino, M. Hinatsu, Y. Tsukada, J. Fujisawa, ITTC Cooperative Experiments on a Series 60 Model at the Ship Research Institute-Flow Measurements and Resistance Test, 1987.
[29] L. Larsson, F. Stern, M. Visonneau, A Workshop on Numerical Ship Hydrodynamics, Chalmers University of Technology, 2010.
[30] J. Longo, F. Stern, Resistance, sinkage and trim, wave profile, and nominal wake tests and uncertainty assessment for DTMB model 5512, in: Proc 25th American Towing Tank Conference, Iowa, 1998.
[31] A. Olivieri, F. Pistani, A. Avanzini, F. Stern, R. Penna, Towing tank experiments of resistance, sinkage and trim, boundary layer, wake, and free surface flow around a naval combatant INSEAN 2340 model, DTIC Document, Tech. Rep. 2001.
[32] W.J. Kim, D.H. Kim, S. Van, Experimental investigation of local flow around kriso 3600teu container ship model in towing tank, J. Soc. Naval Archit. Korea 37 (2000) 1–10 (in Korea).
[33] W.J. Kim, S.H. Van, D.H. Kim, Measurement of flows around modern commercial ship models, Exp. Fluids 31 (5) (2001) 567–578.
[34] F. Noblesse, D. Hendrix, L. Faul, et al., Simple analytical expressions for the height, location, and steepness of a ship bow wave, J. Ship Res. 50 (4) (2006) 360–370.
[35] F. Noblesse, G. Delhommeau, C. Yang, H.Y. Kim, P. Queutey, Analytical bow waves for fine ship bows with rake and flare, J. Ship Res. 55 (2011) 1–18.
[36] F. Noblesse, G. Delhommeau, M. Guilbaud, C. Yang, The rise of water at a ship stem, J. Ship Res. 52 (2008) 89–101.